Research in Astronomy and Astrophysics, 25:045011 (15pp), 2025 April

https://doi.org/10.1088/1674-4527/adc5e2
CSTR: 32081.14.RAA.adc5e2

Research on the Principle of Multi-perspective Solar Magnetic Field Measurement

Zhi-Ming Zhu[1], Xiao-Yan Leng[1], Yang Guo[1], Chuan Li[1], Zhen Li[1], Xi Lu[2], Fan Huang[2], Wei You[2], Yuan-Yong Deng[3,4], Jiang-Tao Su[3,4], Feng Chen[1], and Hao-Cheng Yu[1]
[1] Shool of Astronomy and Space Science and Key Laboratory of Modern Astronomy and Astrophysics, Nanjing University, Nanjing 210023, China; guoyang@nju.edu.cn
[2] Shanghai Institute of Satellite Engineering, Shanghai 200240, China
[3] National Astronomical Observatories, Chinese Academy of Sciences, Beijing 100101, China
[4] School of Astronomy and Space Sciences, University of Chinese Academy of Sciences, Beijing 100049, China
Received 2024 September 28; revised 2025 March 17; accepted 2025 March 20; published 2025 April 16

Abstract

Solar magnetic field measurements mainly use the Zeeman effect, but this method has two problems, namely, low accuracy of the transverse magnetic field components and a 180° ambiguity. Multi-perspective observations can increase the measurement accuracy and resolve the ambiguity. This study investigates how combined observations from the Sun-Earth L5 point, Sun-Earth line, and solar polar-orbiting satellites improve the accuracy of the transverse solar magnetic field under different satellite positional configurations. A three-satellite model is developed using spherical trigonometry to establish coordinate relationships, and the error propagation formulas are applied to correct transverse field measurement errors. The magnetic field measurement error distribution of the Helioseismic and Magnetic Imager is analyzed, and the magnetograms from the three satellites are simulated. The improvement to the transverse field accuracy under various satellite configurations is then assessed based on simulation results. The results show that multi-perspective measurements can reduce transverse component errors ΔB_x to approximately 10% and ΔB_y to about 15% compared to the error from a single satellite. An optimally designed polar orbit can decrease the transverse field error by nearly an order of magnitude for 80% of its operation time.

Key words: Sun: magnetic fields – Sun: photosphere – methods: statistical – space vehicles

1. Introduction

The solar atmosphere is a vast magnetized plasma environment permeated with magnetic fields. The evolution of the solar magnetic field plays a crucial role in heating and ejecting plasma in the solar atmosphere, which in turn triggers space weather events such as solar flares and coronal mass ejections (Solanki et al. 2006). These hazardous space weather events can severely impact human society, particularly on high-tech systems such as aerospace, navigation, communication, and power transmission (Deng et al. 2020; Li & Tian 2022). Studying the solar magnetic field aids in predicting solar activities, thus mitigating or avoiding their potentially disastrous effects on humanity. Moreover, it offers valuable insights into understanding explosive magnetic activities in other stars (Karoff et al. 2016).

Solar activities that cause dramatic changes in space weather are predominantly related to variations in the solar coronal magnetic field (Wiegelmann & Sakurai 2021). However, a significant challenge remains in the lack of effective methods to directly measure the coronal magnetic field. Typically, it is necessary to rely on measurements of the magnetic field in the photosphere as boundary conditions and extrapolate the coronal magnetic field using magnetic field models (Zhu & Wiegelmann 2018; Wiegelmann & Sakurai 2021). Thus, enhancing the accuracy of photospheric magnetic field measurements is crucial for thoroughly understanding the structure and dynamics of the coronal magnetic field.

Observing the solar magnetic field through polarization measurements is one of the most critical research methods in solar physics and space physics (Stenflo 2017). Currently, measurements of the photospheric magnetic field primarily rely on the Zeeman effect, which infers the properties of the magnetic field through polarization measurements of light (Zeeman 1897; Dong & Hu 2019). There are already some instruments working on this principle, such as the Helioseismic and Magnetic Imager (HMI) using the Very Fast Inversion of the Stokes Vector (VFISV; Ye 1987; Borrero et al. 2011) method to obtain magnetic field information, and the Polarimetric and Helioseismic Imager (PHI) also based on polarization information to measure the solar magnetic field (Solanki et al. 2020). However, the Zeeman effect method of measuring magnetic fields has inherent flaws, especially for the transverse component of the magnetic field, and there are two problems: (1) There is a 180° ambiguity in the transverse component of magnetic field (Metcalf 1994); (2) The error of the transverse

component of the magnetic field is one order of magnitude higher than that of the longitudinal component (Ji et al. 2019).

Using methods based on hypotheses and theoretical models, such as the minimum energy principle (Leka et al. 2009; Wang et al. 2019), the transverse magnetic field direction can be determined, thereby eliminating the 180° ambiguity. However, these methods rely on the reliability of the hypotheses and theoretical models and still need to introduce observations independent of the Zeeman effect as verification (Wang 1994). One new idea is to use multiple satellites to simultaneously observe the Sun from different perspectives. This method solves both problems at the same time. Studies have shown that the 180° ambiguity is significantly reduced in the case of dual-satellite observation (Zhou et al. 2021), and the error of one of the transverse components of the magnetic field is reduced to a level close to the error of the longitudinal component (Zeng et al. 2024).

Despite the numerous challenges associated with deploying satellites beyond the Sun-Earth line, including the demanding requirements for launch, orbit insertion, and operational lifespan, the improved accuracy of photospheric magnetic field measurements achieved through multi-perspective observations remains highly valuable. The successful launch and operation of the Solar Orbiter (SO; Müller et al. 2020), which marks the era of multi-perspective observation in solar magnetic field studies (Valori et al. 2022), provides possibilities for this program. China's Advanced Space-based Solar Observatory (ASO-S) provides a new platform for space-based observations of the solar magnetic field (Deng et al. 2019; Gan et al. 2019). Furthermore, the LAgrange-V Solar Observatory (LAVSO) is scheduled to be launched to the Sun-Earth L5 Lagrange point, which, combined with near-Earth observations, aims to achieve a three-dimensional reconstruction of solar activity phenomena (Fang et al. 2024). These devices and projects will provide data support for tri-perspective stereoscopic measurements of the solar magnetic field, significantly reducing the error of the transverse magnetic field component. In the future, possible solar polar orbit observations, near-Sun observations and circum-Solar panoramic observations (Yang et al. 2022; Deng et al. 2023; Wang et al. 2023) will further improve the accuracy of solar magnetic field measurements and help human understanding of solar activity and its impact on the Earth's environment. Therefore, it is necessary to study the principle and effect of multi-perspective measurement to reduce the error of solar magnetic field measurement.

This paper will consider the joint observations from the Sun-Earth line, L5 point, and solar polar-orbiting satellites to improve the measurement accuracy of the transverse solar magnetic field components and address the current issue of inaccurate measurement of the transverse components of the solar magnetic field. The specific research will involve deriving a multi-perspective measurement formula based on the general positional relationships of the three satellites, utilizing existing solar magnetic field observational data from HMI. We will discuss how the joint observations from the Sun-Earth line, L5 point, and solar polar-orbiting satellites can reduce the error in transverse field measurements and validate their feasibility through numerical simulation. Additionally, we will establish a multi-perspective measurement model for the polar orbit satellite under orbital motion, using typical satellite orbits such as SO and Solar Polar-orbit Observatory (SPO; Deng et al. 2023) as examples to verify the effectiveness of the tri-perspective measurement in practical applications and speculate on the optimal satellite orbit configuration. Finally, we will also briefly discuss the impact of the Wilson effect on multi-perspective measurement errors. The content of this paper includes: Section 2, deriving the general formula for tri-perspective measurement, using spherical trigonometry and celestial mechanics to derive the relationship between the observation coordinates of the Earth, L5 point, and polar orbit satellites, and calculating the improved transverse field error of the Earth through the standard deviation propagation formula; Section 3, statistically analyzing the distribution of solar magnetic field errors with heliocentric angle, simulating three magnetic maps as observation data for the Earth, L5 point, and polar orbit satellites, and plugging them into the formula from Section 2 for calculation; Section 4, drawing conclusions based on the simulation results, and discussing the possible impacts brought by other error sources such as the Wilson effect.

2. Theoretical Model

2.1. General Situation of Three-satellite Multi-perspective Measurement

As illustrated in Figure 1, the multi-perspective measurement system comprises the L1 point satellite L_1, the L5 point satellite L_5, and the solar polar orbit satellite S_p. The magnetic map in the lower half of Figure 1 displays the area jointly observed by the three satellites. We will first derive the general formula for multi-perspective measurement from the general relative positional relationships among the three satellites.

Considering the use of three satellites for multi-perspective measurement, the spatial magnetic field vectors they observe can be denoted as $\boldsymbol{B}_i = (B_{z,i}, B_{x,i}, B_{y,i})$, $i = 1, 2, 3$. Here, the z direction represents the magnetic field along each satellite's line of sight, namely the longitudinal component, while the x and y directions represent the transverse components. For the measurement of the spatial vector magnetic field at the same point, the general relationship of the magnetic field components observed by the three satellites can be expressed in matrix form as: $\boldsymbol{B}_1 = \mathcal{R}_{12}\boldsymbol{B}_2 = \mathcal{R}_{13}\boldsymbol{B}_3$. Expanding this equation yields:

$$\begin{bmatrix} B_{z,1} \\ B_{x,1} \\ B_{y,1} \end{bmatrix} = \begin{bmatrix} a_{11} & a_{12} & a_{13} \\ a_{21} & a_{22} & a_{23} \\ a_{31} & a_{32} & a_{33} \end{bmatrix} \begin{bmatrix} B_{z,2} \\ B_{x,2} \\ B_{y,2} \end{bmatrix} = \begin{bmatrix} b_{11} & b_{12} & b_{13} \\ b_{21} & b_{22} & b_{23} \\ b_{31} & b_{32} & b_{33} \end{bmatrix} \begin{bmatrix} B_{z,3} \\ B_{x,3} \\ B_{y,3} \end{bmatrix}. \quad (1)$$

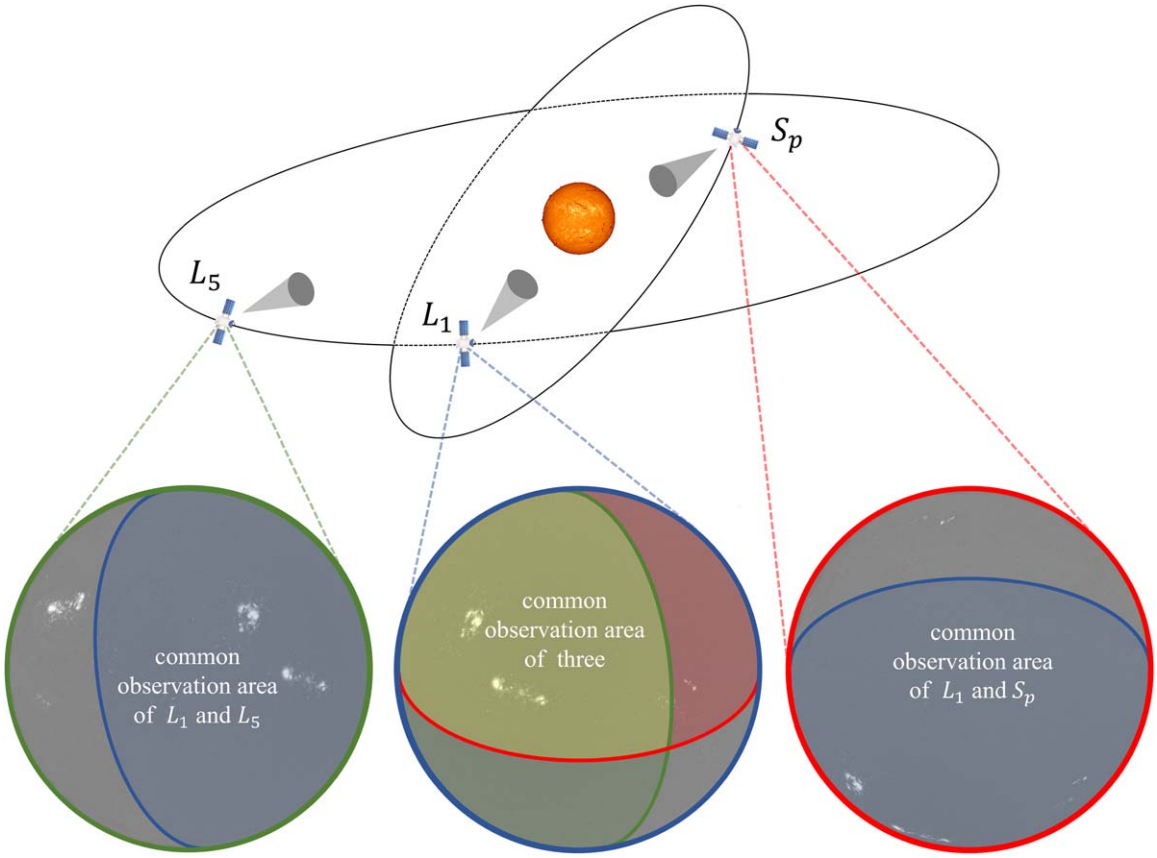

Figure 1. Diagram of the tri-perspective measurement. Blue, green, and red respectively represent the solar magnetic maps observed from the perspectives of the L1 point satellite L_1, the L5 point satellite L_5, and the solar polar orbit satellite S_p. The yellow area in the middle signifies the region jointly observed by all three satellites.

From this, six equations regarding all nine magnetic field components can be obtained:

$$B_{x,1} = a_{21}B_{z,2} + a_{22}B_{x,2} + a_{23}B_{y,2}, \tag{2}$$

$$B_{x,1} = b_{21}B_{z,3} + b_{22}B_{x,3} + b_{23}B_{y,3}, \tag{3}$$

$$B_{y,1} = a_{31}B_{z,2} + a_{32}B_{x,2} + a_{33}B_{y,2}, \tag{4}$$

$$B_{y,1} = b_{31}B_{z,3} + b_{32}B_{x,3} + b_{33}B_{y,3}, \tag{5}$$

$$B_{z,1} = a_{11}B_{z,2} + a_{12}B_{x,2} + a_{13}B_{y,2}, \tag{6}$$

$$B_{z,1} = b_{11}B_{z,3} + b_{12}B_{x,3} + b_{13}B_{y,3}. \tag{7}$$

We assume that $a_{13}b_{13} \neq 0$. Since the case where $a_{13}b_{13} = 0$ can be resolved by reorienting the x and y axes in the coordinate system, this assumption does not affect the derivation for the general case. As we will see in Section 2.2, when certain elements of the rotation matrix $\mathcal{R}_{12}$ and $\mathcal{R}_{13}$, as well as some of their linear combinations, approach zero, it indicates a scenario where the three-satellite multi-perspective measurement method has a less effective improvement in accuracy. From Equations (6) and (7), we obtain:

$$B_{y,2} = \frac{1}{a_{13}}(B_{z,1} - a_{11}B_{z,2} - a_{12}B_{x,2}), \tag{8}$$

$$B_{y,3} = \frac{1}{b_{13}}(B_{z,1} - b_{11}B_{z,3} - b_{12}B_{x,3}). \tag{9}$$

Substituting Equations (8) and (9) into Equations (2), (4), (3) and (5) eliminates all y-direction magnetic field components:

$$a_{21}B_{z,2} + a_{22}B_{x,2} + \frac{a_{23}}{a_{13}}(B_{z,1} - a_{11}B_{z,2} - a_{12}B_{x,2})$$

$$= b_{21}B_{z,3} + b_{22}B_{x,3} + \frac{b_{23}}{b_{13}}(B_{z,1} - b_{11}B_{z,3} - b_{12}B_{x,3}), \tag{10}$$

$$a_{31}B_{z,2} + a_{32}B_{x,2} + \frac{a_{33}}{a_{13}}(B_{z,1} - a_{11}B_{z,2} - a_{12}B_{x,2})$$

$$= b_{31}B_{z,3} + b_{32}B_{x,3} + \frac{b_{33}}{b_{13}}(B_{z,1} - b_{11}B_{z,3} - b_{12}B_{x,3}). \tag{11}$$

Rearranging, we obtain a system of linear equations for $B_{x,2}$ and $B_{x,3}$:

$$\begin{bmatrix} a_{13}a_{22}b_{13} - a_{12}a_{23}b_{13} & a_{13}b_{12}b_{23} - a_{13}b_{13}b_{22} \\ a_{13}a_{32}b_{13} - a_{12}a_{33}b_{13} & a_{13}b_{12}b_{33} - a_{12}a_{23}b_{13} \end{bmatrix} \begin{bmatrix} B_{x,2} \\ B_{x,3} \end{bmatrix}$$
$$= \begin{bmatrix} (a_{13}b_{23} - a_{23}b_{13})B_{z,1} - (a_{21}a_{13}b_{13} - a_{11}a_{23}b_{13})B_{z,2} + (a_{13}b_{13}b_{21} - a_{13}b_{11}b_{23})B_{z,3} \\ (a_{13}b_{33} - a_{33}b_{13})B_{z,1} - (a_{31}a_{13}b_{13} - a_{11}a_{33}b_{13})B_{z,2} + (a_{13}b_{13}b_{31} - a_{13}b_{11}b_{33})B_{z,3} \end{bmatrix}. \quad (12)$$

Defining coefficients:

$$\begin{aligned} C_0 &= b_{13}[(b_{13}b_{32} - b_{12}b_{33})(a_{13}a_{22} - a_{12}a_{23}) \\ &\quad + (b_{13}b_{22} - b_{12}b_{23})(a_{13}a_{32} - a_{12}a_{33})], \\ C_1^* &= (b_{13}b_{32} - b_{12}b_{33})(a_{13}b_{23} - a_{23}b_{13}) \\ &\quad + (b_{13}b_{22} - b_{12}b_{23})(a_{13}b_{33} - a_{33}b_{13}), \\ C_2^* &= -(b_{13}b_{32} - b_{12}b_{33})(a_{21}a_{13}b_{13} - a_{11}a_{23}b_{13}) \\ &\quad - (b_{13}b_{22} - b_{12}b_{23})(a_{13}a_{31}b_{13} - a_{11}a_{33}b_{13}), \\ C_3^* &= (b_{13}b_{32} - b_{12}b_{33})(a_{13}b_{13}b_{21} - a_{13}b_{11}b_{23}) \\ &\quad + (b_{13}b_{22} - b_{12}b_{23})(a_{13}b_{13}b_{31} - a_{13}b_{11}b_{33}), \\ C_i &= \frac{C_i^*}{C_0},\ i = 1, 2, 3, \end{aligned} \quad (13)$$

we solve Equation (12) to obtain

$$B_{x,2} = C_1 B_{z,1} + C_2 B_{z,2} + C_3 B_{z,3}. \quad (14)$$

Given that, in the previous assumption, the positional relationships of the three satellites do not possess any special characteristics, the second satellite can represent the general case of the satellite whose accuracy is to be improved. Therefore, it is unnecessary to further calculate $B_{x,1}$ and $B_{x,3}$. This provides the general expression for calculating the x-direction magnetic field component of one satellite using the longitudinal components measured by the three satellites in the multi-perspective measurement system. For the independent variables x and y, we have the formula for error propagation

$$\Delta F(x, y)^2 = \Delta x^2 \left(\frac{\partial F}{\partial x}\right)^2 + \Delta y^2 \left(\frac{\partial F}{\partial y}\right)^2. \quad (15)$$

Since the longitudinal magnetic field components observed by each of the three satellites are independent, we can substitute Equation (14) into the previous equation to obtain the error $\Delta B_{x,2}$ improved by multi-perspective measurement accuracy

$$\Delta B_{x,2} = \sqrt{C_1^2 \Delta B_{z,1}^2 + C_2^2 \Delta B_{z,2}^2 + C_3^2 \Delta B_{z,3}^2}. \quad (16)$$

Similarly, we can derive the general formula for calculating the y-direction magnetic field component as follows:

$$B_{y,2} = D_1 B_{z,1} + D_2 B_{z,2} + D_3 B_{z,3}, \quad (17)$$

$$\Delta B_{y,2} = \sqrt{D_1^2 \Delta B_{z,1}^2 + D_2^2 \Delta B_{z,2}^2 + D_3^2 \Delta B_{z,3}^2}, \quad (18)$$

where the coefficients are:

$$\begin{aligned} D_0 &= b_{12}[(b_{12}b_{33} - b_{13}b_{32})(a_{12}a_{23} - a_{13}a_{22}) \\ &\quad + (b_{12}b_{23} - b_{13}b_{22})(a_{12}a_{33} - a_{13}a_{32})], \\ D_1^* &= (b_{13}b_{33} - b_{13}b_{32})(a_{12}b_{22} - a_{22}b_{12}) \\ &\quad + (b_{12}b_{23} - b_{13}b_{22})(a_{12}b_{32} - a_{32}b_{12}), \\ D_2^* &= -(b_{12}b_{33} - b_{13}b_{32})(a_{21}a_{12}b_{12} - a_{11}a_{22}b_{12}) \\ &\quad - (b_{12}b_{23} - b_{13}b_{22})(a_{12}a_{31}b_{12} - a_{11}a_{32}b_{12}), \\ D_3^* &= (b_{12}b_{33} - b_{13}b_{32})(a_{12}b_{12}b_{21} - a_{12}b_{11}b_{22}) \\ &\quad + (b_{12}b_{23} - b_{13}b_{22})(a_{12}b_{12}b_{31} - a_{12}b_{11}b_{32}), \\ D_i &= \frac{D_i^*}{D_0},\ i = 1, 2, 3. \end{aligned} \quad (19)$$

Thus, we have obtained the general formula for calculating the transverse field and its error using longitudinal field measurements in the three-satellite multi-perspective measurement method.

2.2. Polar Orbit Satellite Model with Earth as the Reference Point

Next, let us consider a specific application scenario: a three-satellite multi-perspective measurement system consisting of satellites located at the L1 point, the L5 point, and in a polar orbit. Previous work by Zeng et al. (2024) has shown us that joint observations by the L5 point satellite and the L1 point satellite can significantly improve the accuracy of transverse field measurements parallel to the solar equatorial plane, specifically, the x-direction component in the Earth observation coordinate system. The components perpendicular to both the x-direction and the line of sight are defined as the y-component.

To further validate how the three-satellite system enhances the measurement accuracy of the y-component for the L1 point satellite, we have two approaches: (1) Using the polar orbit satellite and the L1 point satellite for joint observation and calculating the magnetic field y-component error through a dual-satellite multi-perspective measurement method; (2) Utilizing all three satellites and calculating the magnetic field y-component error through the three-satellite multi-perspective measurement method. Here, we will roughly compare the effectiveness of both approaches in improving accuracy under an ideal model.

Based on the actual situation, we construct a celestial sphere diagram for the three satellites. Figure 2 illustrates the relationship between the observation coordinate systems of the three satellites under actual solar conditions. It is noteworthy that the circle representing the polar orbit satellite S_p is not its actual orbit but merely an auxiliary circle

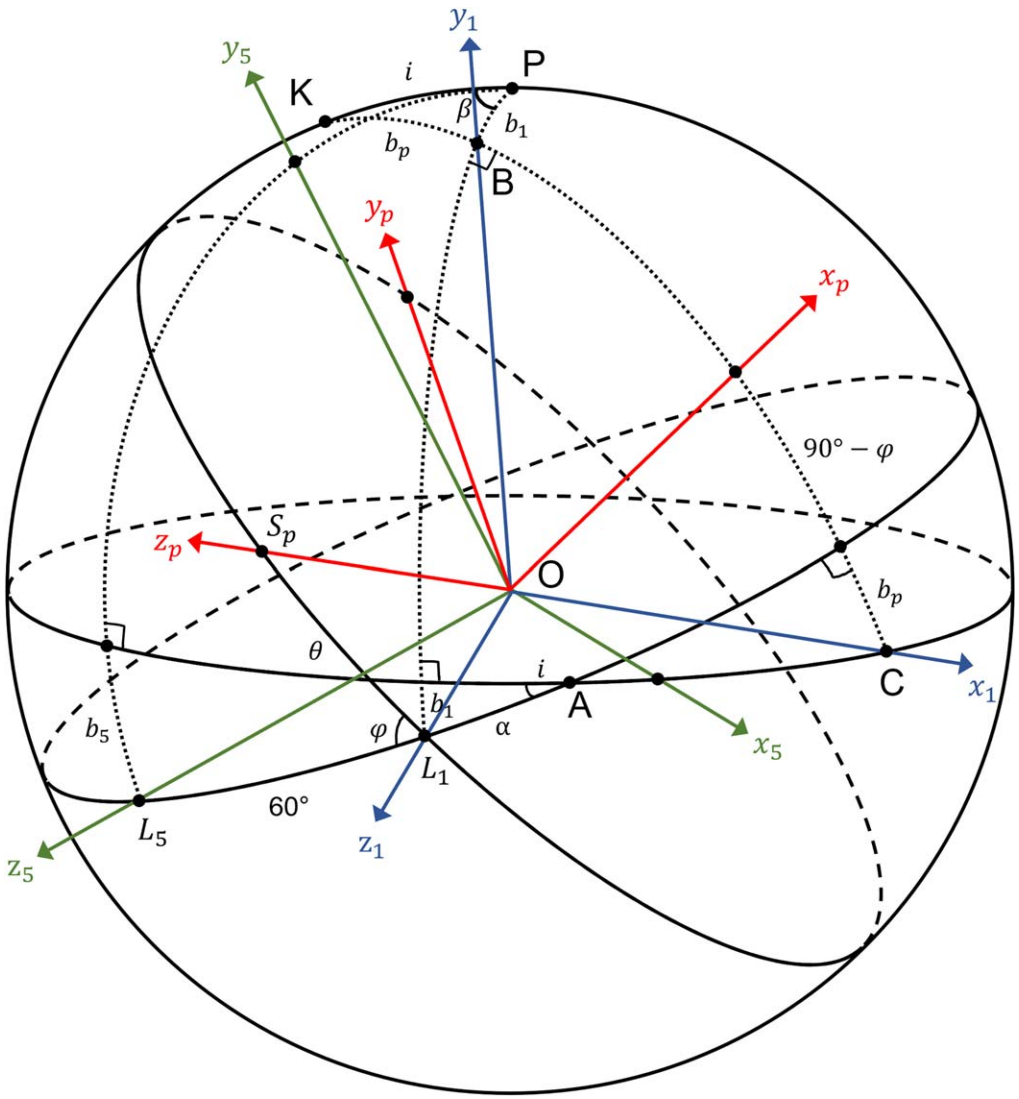

Figure 2. A celestial sphere with the Sun at the center. Here, P is the north celestial pole of the Sun, and K is the north ecliptic pole. O-$x_1y_1z_1$, O-$x_5y_5z_5$ and O-$x_py_pz_p$ are the observation coordinate systems for Earth (L_1 point), the L_5 point, and the polar orbit satellite S_p, respectively. O-$x_1y_1z_1$ intersects the spherical surface at point L_1, point B and point C. b_1 is the inclination angle between Earth and the solar equatorial plane, b_5 is the inclination angle between the L_5 point and the solar equatorial plane, and b_p is the inclination angle between the x_1 axis and the ecliptic plane. β is the angle formed by Earth, the north celestial pole of the Sun, and the L_5 point. α is the ecliptic longitude of Earth (starting from point A, counterclockwise as positive). φ is the angle formed by the polar orbit satellite, Earth, and the L_5 point. θ denotes the angular distance between Earth and the polar orbit satellite, and i is the angle between the solar equator and the ecliptic.

constructed when Earth is taken as the reference point, characterized by parameters (φ, θ) to denote the position of the polar orbit satellite. This selection of coordinate system facilitates the subsequent calculation of the rotation matrix.

Following the previous section, let $\boldsymbol{B}_{L5} = \mathcal{R}_{12}\boldsymbol{B}_{L1} = \mathcal{R}_{13}\boldsymbol{B}_{Sp}$, then we only need to determine the specific forms of the rotation matrices $\mathcal{R}_{12} = (a_{ij})$ and $\mathcal{R}_{13} = (b_{ij})$ to apply the general formula for the three-satellite method. For the dual-satellite method, we need to determine the specific form of the rotation matrix $\mathcal{R}_{23} = (d_{ij})$ in $\boldsymbol{B}_{L1} = \mathcal{R}_{23}\boldsymbol{B}_{Sp}$.

Referring to the work of Zeng et al. (2024), it is easy to obtain the values of b_1, b_5 and β. Note that b_1 is positive when the Earth is north of the solar equator and negative when south, and similarly for b_5. Thus, we have

$$\boldsymbol{B}_{L5} = \mathcal{R}_x(-b_5)\mathcal{R}_y(-\beta)\mathcal{R}_x(b_1)\boldsymbol{B}_{L1} = \mathcal{R}_{12}\boldsymbol{B}_{L1}. \quad (20)$$

Among them, $\mathcal{R}_z(\alpha)$, $\mathcal{R}_x(\alpha)$ and $\mathcal{R}_y(\alpha)$ respectively represent the rotation matrices for counterclockwise rotation by an angle of α around the z-axis, x-axis and y-axis. The specific

definitions are as follows:

$$\mathcal{R}_z(\alpha)=\begin{bmatrix}1 & 0 & 0\\ 0 & \cos\alpha & -\sin\alpha\\ 0 & \sin\alpha & \cos\alpha\end{bmatrix}\mathcal{R}_x(\alpha)=\begin{bmatrix}\cos\alpha & 0 & \sin\alpha\\ 0 & 1 & 0\\ -\sin\alpha & 0 & \cos\alpha\end{bmatrix}$$
$$\mathcal{R}_y(\alpha)=\begin{bmatrix}\cos\alpha & -\sin\alpha & 0\\ \sin\alpha & \cos\alpha & 0\\ 0 & 0 & 1\end{bmatrix}. \tag{21}$$

Since the three vertices of $\Delta L_{1\mathrm{BC}}$ are respectively the three intersection points of the coordinate axes and the spherical surface, $\angle L_{1\mathrm{BC}}$ is a right angle. From this, it can be known that $\angle$PBK is also a right angle. Using the cosine rule for sides, we have

$$\cos i=\cos b_1\cos b_p+\sin b_1\sin b_p\cos\angle\mathrm{PBK}=\cos b_1\cos b_p \tag{22}$$

Therefore, we can solve for b_p as $\cos b_p=\frac{\cos i}{\cos b_1}$. To obtain the relationship between the S_p coordinate system and the L_1 coordinate system, we can first rotate the S_p coordinate system counterclockwise around the x-axis by an angle of θ to align their z-axes, then rotate clockwise around the z-axis by $(90^\circ-\varphi+b_p)$. Therefore, we have:

$$\boldsymbol{B}_{L1}=\mathcal{R}_z(-90^\circ+\varphi-b_p)\mathcal{R}_x(\theta)\boldsymbol{B}_{Sp}=\mathcal{R}_{23}\boldsymbol{B}_{Sp}, \tag{23}$$

$$\begin{aligned}\boldsymbol{B}_{L5}&=\mathcal{R}_{12}\mathcal{R}_{23}\boldsymbol{B}_{Sp}\\ &=\mathcal{R}_{12}\mathcal{R}_z(-90^\circ+\varphi-b_p)\mathcal{R}_x(\theta)\boldsymbol{B}_{Sp}\\ &=\mathcal{R}_x(-b_5)\mathcal{R}_y(-\beta)\mathcal{R}_x(b_1)\mathcal{R}_z(-90^\circ+\varphi-b_p)\mathcal{R}_x(\theta)\boldsymbol{B}_{Sp}\\ &=\mathcal{R}_{13}\boldsymbol{B}_{Sp}.\end{aligned} \tag{24}$$

At this point, we only need to provide the specified parameters for the polar orbit satellite, φ and θ, to calculate the specific values of (a_{ij}), (b_{ij}) and (d_{ij}).

From the dual-satellite method, we obtain the formula for $\Delta B_{y,L1}$ as

$$\Delta B_{y,L1}=\sqrt{(d_{21}-Cd_{11})^2\Delta B_{z,Sp}^2+(d_{22}-Cd_{12})^2\Delta B_{x,Sp}^2+(d_{23}-Cd_{13})^2\Delta B_{y,Sp}^2+C^2\Delta B_{z,L1}^2}. \tag{25}$$

The coefficient C can be determined by the following equation

$$C=\frac{d_{21}d_{11}\Delta B_{z,Sp}^2+d_{22}d_{12}\Delta B_{x,Sp}^2+d_{23}d_{13}\Delta B_{y,Sp}^2}{d_{11}^2\Delta B_{z,Sp}^2+d_{12}^2\Delta B_{x,Sp}^2+d_{13}^2\Delta B_{y,Sp}^2+\Delta B_{z,L1}^2}. \tag{26}$$

Comparing Equations (25) with (18), it is noteworthy that the advantage of the three-satellite method lies in the fact that it does not require introducing horizontal field components into the calculations. Since the measurement precision of vertical field components is typically one order of magnitude higher than that of horizontal field components, the magnetic field y-component error obtained from the three-satellite method formula should theoretically be smaller. However, a potential drawback of the three-satellite method formula is that in certain special satellite relative positioning scenarios, C_0 or D_0 (defined in Equations (13) and (19) respectively) may approach 0, leading to the error tending toward infinity.

Assuming the instruments used by the three satellites are identical, and the measurement errors of each magnetic field component are uniformly distributed over the solar disk, let $\Delta B_x=\Delta B_y=\alpha\Delta B_z$. Here we tentatively ignore the differences in magnetic field errors at different positions on the solar disk and only consider the mean value of the errors on the solar disk. We define $\mu=\frac{\Delta B_{\mathrm{new}}}{\Delta B}$ as the ratio of the magnetic field error after precision enhancement through multi-perspective measurement to the original error, and similarly, $\mu_y=\frac{\Delta B_{y,\mathrm{new}}}{\Delta B_y}$. When $\alpha=12$, the comparison of the effect of improving the precision of the y-component between the two is shown in Figure 3.

Figure 3 constrains $\mu\leqslant 1$. In reality, $\mu_{y,3}$ is significantly greater than 1 in some red regions. However, since the regions where μ exceeds 1 do not contribute to an improvement in accuracy, specific numerical values need not be displayed. Hence, all μ values greater than 1 are set to 1. Despite the existence of these regions where μ significantly exceeds 1 in the three-satellite method, it is still visually apparent from Figure 3 that in the vast majority of cases, the three-satellite method outperforms the dual-satellite method. In regions where the performance of the three-satellite method is poorer, the value of $\mu_{y,2}$ in the dual-satellite method is also close to 1. Observing the (φ,θ) in these regions reveals that polar orbit satellites inherently struggle to provide high-precision observations of the y-direction component under the L_1 viewpoint. If the better performing result from either method can always be chosen at each polar orbit satellite position, it is possible to retain the superior accuracy improvement effect of the three-satellite method while avoiding situations where errors tend toward infinity in certain regions. This method is referred to as the comprehensive method.

In addition to the accuracy improvement effect, it is also necessary to pay attention to the size of the area where multiple satellites can make joint observations. For example, in the dual-satellite measurement shown in the upper left corner in Figure 3, when θ is close to 180°, there is almost no area where two satellites can observe at the same time.

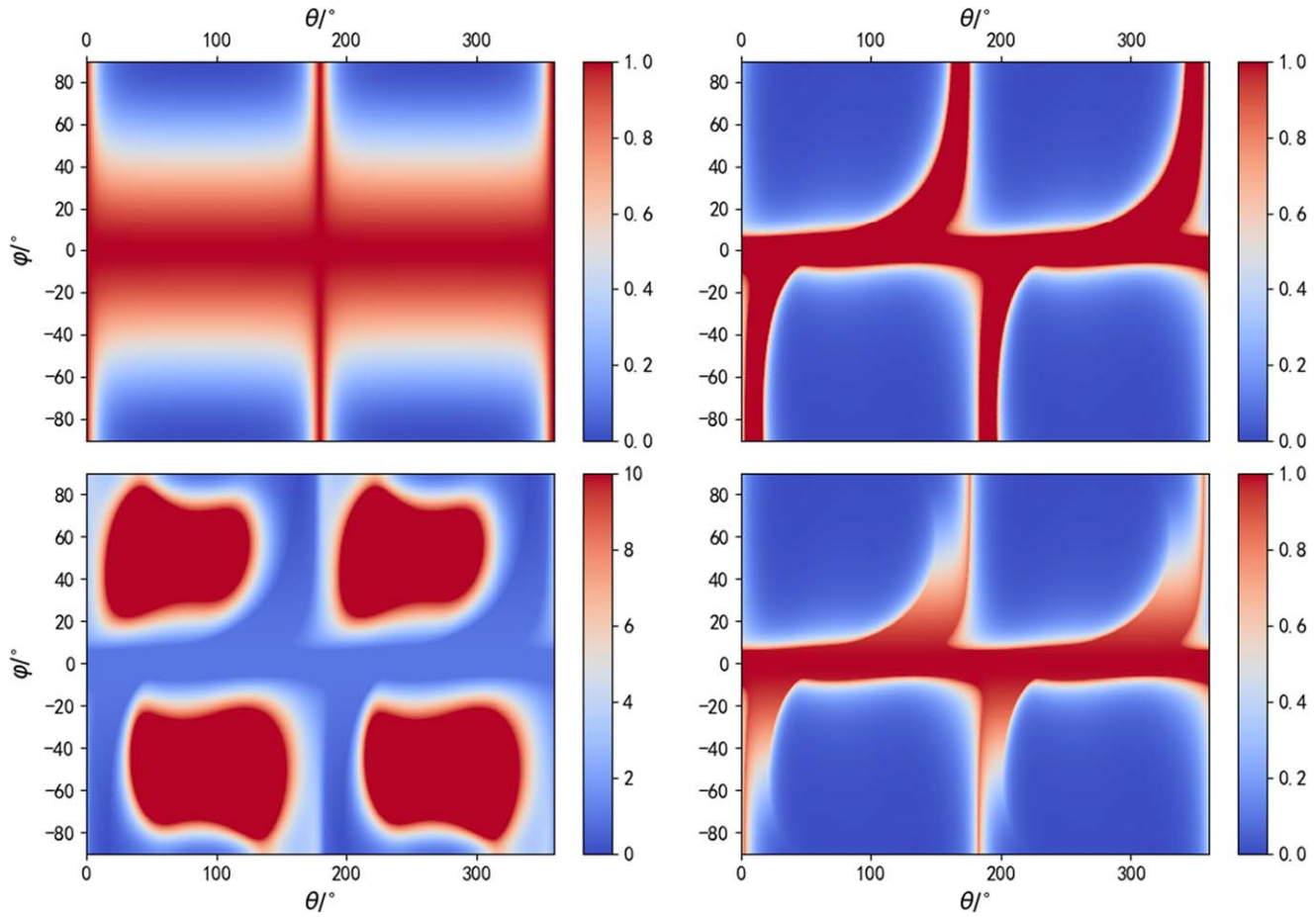

Figure 3. When conducting multi-perspective measurements at different positions of the polar orbit satellite, the reduction in magnetic field y-component error. φ represents the angle formed by the polar orbit satellite S_p, the Earth, and L_5; θ represents the angular distance between the Earth and S_p. Top Left: $\mu_{y,2}$ for the dual-satellite measurement method. Top Right: $\mu_{y,3}$ for the three-satellite measurement method. Bottom Left: The ratio of errors between the two methods $\frac{\mu_{y,2}}{\mu_{y,3}}$. Bottom Right: μ_y for the comprehensive method, which always selects the better method between the dual-satellite and three-satellite methods at each point.

2.3. Polar Orbit Satellite Model Represented by the Orbital Elements

In practical applications, we are also concerned with the variation in accuracy improvement as satellites move along their orbits. For a three-satellite multi-perspective measurement system consisting of satellites at the L1 point, the L5 point, and in polar orbit, the positional parameters (φ, θ) of the polar orbit satellite do not intuitively reflect its orbital dynamics. Therefore, we need to select a new set of parameters related to the orbital elements of the polar orbit satellite.

In general, a satellite has six orbital elements: the semimajor axis a, eccentricity e, inclination γ, R.A. of the ascending node Ω, argument of perigee ω, and true anomaly f.

For convenience in discussion, we fix the orbital ascending node at point A, which is the intersection of the solar equator and the ecliptic, thus eliminating the need for the parameter Ω. Since the accuracy improvement in multi-perspective measurement depends on the relative positions of the three satellites rather than their absolute positions, and the relative positions can be altered by changing the initial angular separation α_0 between the Earth and point A, this assumption does not affect the subsequent discussion on the accuracy improvement. The celestial sphere diagram under this condition is depicted in Figure 4.

Let the Earth's orbital period be 365.25 days, and the time variable t be measured in days. The Earth's ecliptic longitude is given by $\alpha(t) = \alpha_0 + \frac{2\pi}{365.25}t$, where α_0 is a constant representing the initial ecliptic longitude of the Earth. The inclination angle $b_1(t)$ of the x_1 axis with respect to the ecliptic plane is $b_1(t) = \sin i \cdot \sin \alpha(t)$. The angular separation between the polar orbit satellite and the ascending node A is $\theta(t) = \omega + f(t)$, where ω is the argument of perigee, and f is the true anomaly, which can be determined by the

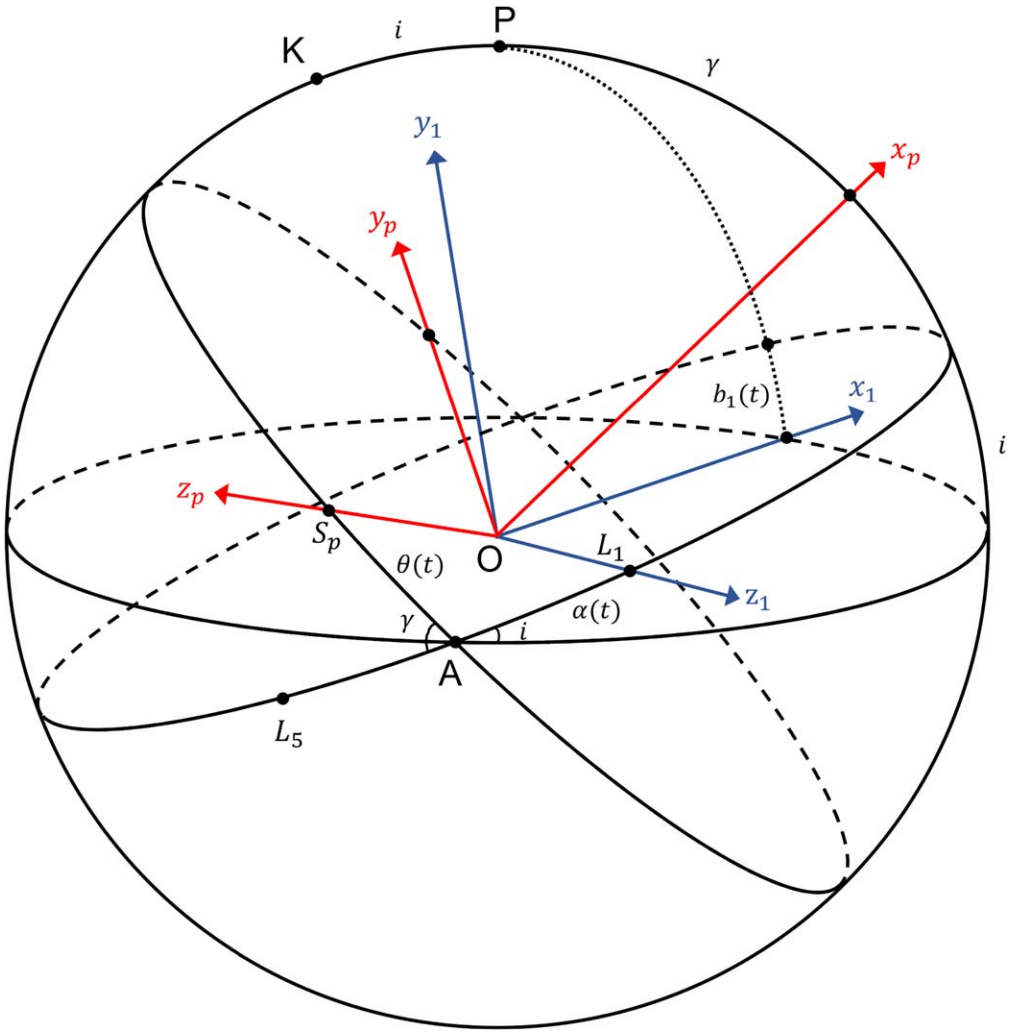

Figure 4. The celestial sphere diagram depicts the orbit of the polar orbit satellite in relation to the solar celestial sphere. Here, P is the north celestial pole of the Sun, K is the north ecliptic pole, and A is the intersection of the solar equator and the ecliptic, which is also the ascending node for the polar orbit satellite. O-$x_1y_1z_1$ and O-$x_py_pz_p$ are the observation coordinate systems for Earth (L_1 point) and the polar orbit satellite S_p, respectively. b_1 is the inclination angle between the x_1 axis and the ecliptic plane. α is the ecliptic longitude of Earth (starting from point A, counterclockwise as positive). γ is the inclination angle of the polar orbit satellite's orbit. $\theta = f + \omega$ is the angular separation between the polar orbit satellite and the ascending node A, and i is the angle between the solar equator and the ecliptic.

following equation

$$\frac{df}{dt} = \frac{\sqrt{GM_\odot}}{[a(1-e^2)]^{\frac{3}{2}}}(1+e\cos f)^2\,. \tag{27}$$

In the equation, a represents the semimajor axis of the orbit, e denotes the eccentricity of the orbit, G is the gravitational constant, and $M_\odot$ stands for the mass of the Sun.

Continuing with the approach from Section 2.2, the determination of $\mathcal{R}_{12} = (a_{ij})$ remains unchanged, with the only addition being the introduction of the variable t. Regarding $\mathcal{R}_{13} = (b_{ij})$ and $\mathcal{R}_{23} = (d_{ij})$, it is necessary to reconsider the relationship between the S_p coordinate system and the L_1 coordinate system. First, the S_p coordinate system is rotated counterclockwise about the x-axis by θ to align its z-axis with point A. Then, it is further rotated clockwise about the z-axis by $(90^\circ - \gamma)$ to align its x-axis with the ecliptic plane. Subsequently, a counterclockwise rotation about the y-axis by α is performed to make their z-axes coincide, followed by a clockwise rotation about the z-axis by b_1. Thus, we have:

$$\boldsymbol{B}_{L1} = \mathcal{R}_z(b_1)\mathcal{R}_y(\alpha)\mathcal{R}_z(-90^\circ+\gamma)\mathcal{R}_x(\theta)\boldsymbol{B}_{Sp} = \mathcal{R}_{23}\boldsymbol{B}_{Sp}, \tag{28}$$

$$\begin{aligned}\boldsymbol{B}_{L5} &= \mathcal{R}_{12}\mathcal{R}_{23}\boldsymbol{B}_{Sp}\\ &= \mathcal{R}_{12}\mathcal{R}_z(b_1)\mathcal{R}_y(\alpha)\mathcal{R}_z(-90^\circ+\gamma)\mathcal{R}_x(\theta)\boldsymbol{B}_{Sp}\\ &= \mathcal{R}_{13}\boldsymbol{B}_{Sp}.\end{aligned} \tag{29}$$

Once the matrices are determined, they can be substituted into the formula for the three-satellite measurement (Equation (18)) and the dual-satellite measurement (Equation (25)).

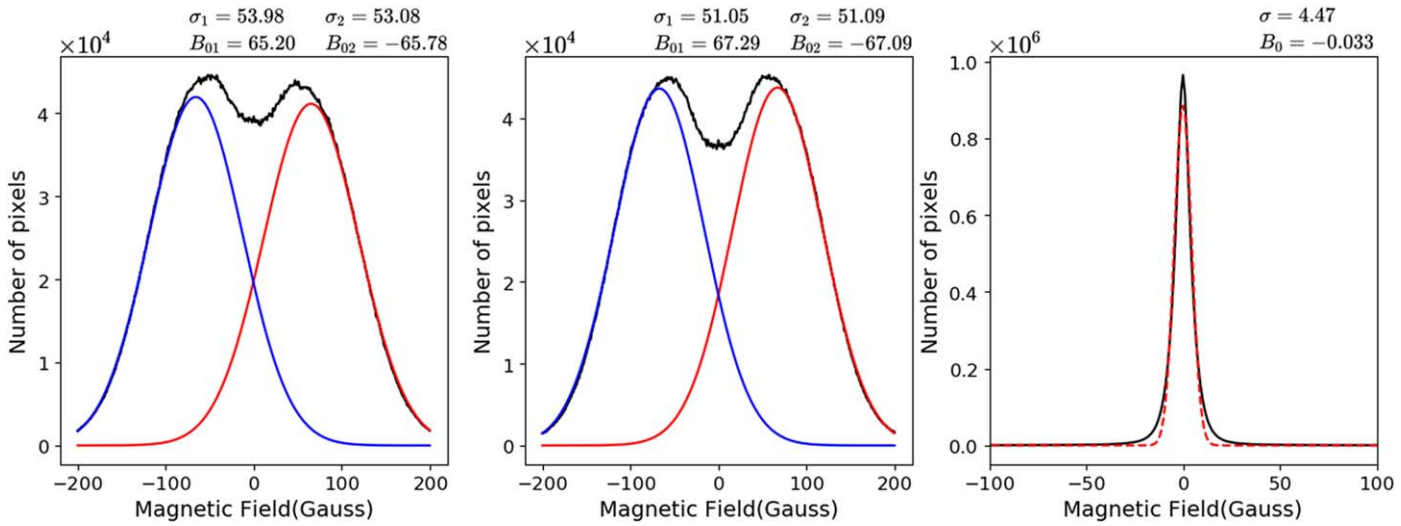

Figure 5. Estimation of measurement errors for the three components of the vector magnetic field. Left: Weak field distribution of B_x with double Gaussian fitting. Middle: Weak field distribution of B_y with double Gaussian fitting. Right: Weak field distribution of B_z with Gaussian fitting. Data sourced from the HMI website, the plots depict the fitting results of magnetic field data at 11:36 UT on 2017 September 6.

This model requires specification of five parameters: α_0, a, e, γ, and ω. From these, a function $\mu(t)$ can be obtained representing the variation of the accuracy improvement as the polar orbit satellite moves along its orbit.

3. Data Simulation and Results

3.1. Vector Magnetic Field Error Distribution Statistics

In the ideal model described in Section 2, we assumed that the measurement errors of magnetic field components are uniformly distributed over the solar disk. However, factors such as the limb darkening effect result in different heliocentric angles corresponding to different magnetic field measurement errors. Therefore, the first step is to statistically analyze the distribution of solar magnetic field errors with respect to heliocentric angles.

Here, we utilize observation data from the Solar Dynamic Observatory (SDO)/HMI instrument to construct statistical histograms of the solar magnetic field in weak fields. Through Gaussian fitting, we estimate the level of magnetic field errors using the standard deviation (Liu et al. 2012).

We select magnetic field data from 2017 September 6, at 11:36 UT. Figure 5 illustrates the statistical histograms of the three components of the weak magnetic field over the solar disk. From Figure 5, it can be observed that the distribution of the B_z component approximately follows a Gaussian distribution. The Gaussian fitting yields a center value of -0.033 G and a standard deviation of 4.47 G, hence we consider $\Delta B_z = 4.47$ G. On the other hand, the distributions of B_x and B_y exhibit bimodal shapes. The fitting results suggest that these distributions can be approximated by double Gaussian distributions, with two centers that are approximately symmetric and with similar standard deviations. We estimate the magnetic field component errors by averaging the standard deviations of the two single-peaked Gaussians. Therefore, we obtain $\Delta B_x = 53.53$ G and $\Delta B_y = 51.07$ G as the estimated errors for the B_x and B_y components, respectively.

From this result, we can further deduce that the error in the transverse component is generally around 12 times that of the error in the vertical component. This also validates the approximation we made in Section 2.2, where we assumed $\Delta B_x = \Delta B_y = 12\Delta B_z$.

By performing distribution statistics and fitting on full-disk magnetic maps at different times, we can derive the temporal variation pattern of measurement errors in the magnetic field observed by the HMI instrument. Figure 6 illustrates the variation of measurement errors for the three magnetic field components as observed by the HMI instrument from 2010 May 1 to 2023 September 27.

Overall, the measurement errors of the three components exhibit a slow increase over time, primarily attributed to instrument aging. A notable discontinuity in instrument precision occurred on 2016 April 13, where the error in the line-of-sight magnetic field, ΔB_z, markedly decreased to approximately 80% of its previous value. Meanwhile, the transverse field error experienced a slight decrease at this juncture, followed by a pronounced trend of annual escalation, with the growth rate of ΔB_x slightly outpacing that of ΔB_y. Additionally, variations in the errors of each magnetic field component exhibit a yearly periodicity, manifesting as an "M"-shaped curve over the course of a year. Subsequently, we will compute the average magnetic field error over the entirety of 2017.

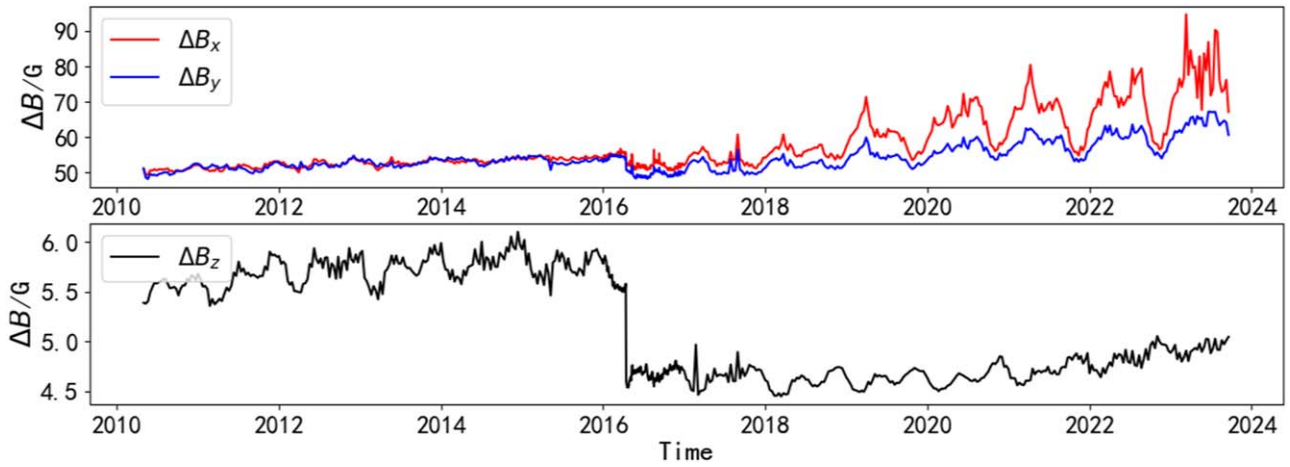

Figure 6. The variation of magnetic field measurement errors of the HMI instrument during the period from 2010 May 1 to 2023 September 17. Upper: the temporal evolution of ΔB_x and ΔB_y. Lower: the temporal evolution of ΔB_z. The data are sourced from the HMI website, with magnetic maps obtained every 10 days starting from 2010 May 1.

For a given heliocentric angle θ, if statistical analysis of the weak-field distribution is confined to the range $(\theta, \theta + d\theta)$, an average error on that heliocentric angle can be derived. However, for uniformly segmented heliocentric angles, the corresponding areas of the circular rings are unequal. Statistical efficacy within smaller area rings is inferior, often resulting in inaccurate fitting or even non-convergence. To ensure better statistical efficacy within each ring, let $x = \sin^2\theta$, revealing that for each infinitesimal area element of the ring

$$\mathrm{d}S = \mathrm{d}(\pi r^2) = \pi \mathrm{d}\left[\left(\frac{r}{R_\odot}\right)^2 R_\odot^2\right] = \pi \mathrm{d}(\sin^2\theta \cdot R_\odot^2) = \pi R_\odot^2 dx. \tag{30}$$

Here r represents the inner radius of the small ring $(\theta, \theta + d\theta)$, and $R_\odot$ denotes the radius of the Sun. Thus, for uniformly spaced dx, the areas of the rings corresponding to heliocentric angles are equal.

Dividing x into 90 equal parts, statistical analysis as described above is conducted on the magnetic field errors of HMI for each day in 2017, resulting in a scatter plot illustrating the distribution of magnetic field errors with respect to heliocentric angles. Given our intention to model the distribution of magnetic field errors using a Gaussian distribution, it is necessary to further compute the standard deviation of the error distribution within each heliocentric angle.

From Figure 7, it can be observed that the errors of all three magnetic field components increase with the heliocentric angle, exhibiting a trend that can be approximately regarded as linear. The overall standard deviation of magnetic field errors also increases with the heliocentric angle, but in the low heliocentric angle region, the error distribution is more scattered. After completing the statistical analysis of solar magnetic field errors with respect to heliocentric angles, the theoretical data simulation for the three-satellite multi-perspective measurement at Earth, L5 point, and polar orbit satellite can commence.

3.2. Data Simulation

Using the average values of magnetic field errors with respect to heliocentric angles as depicted in Figure 7, Gaussian noise is randomly added based on the standard deviation of errors. The average error value of each heliocentric angle serves as the center of the Gaussian distribution, with the standard deviation of errors serving as σ. This method is applied to assign values for heliocentric angles within $x \in \left[0, \frac{80}{90}\right]$, corresponding to a maximum solar angle of approximately 70°.5. For regions with higher heliocentric angles, due to limb darkening effects, the reliability of errors is lower. Therefore, linear regression is performed on the average error values within $x \in \left[0, \frac{80}{90}\right]$, and the results are extrapolated to higher solar angle regions.

Assuming identical characteristics for the three satellites, this method enables the simulation of magnetic field data errors observed by the three satellites. These error estimations are then incorporated into the theoretical model described in Section 2 to assess the enhancement of magnetic field measurement precision by multi-perspective measurements at various positions and orbits of the polar orbit satellite.

3.3. Calculation Results

Based on the work of Zeng et al. (2024), we extend the process of transformation between two magnetic maps to three magnetic maps, namely interpolating the magnetic maps of the L5 satellite and the polar orbit satellite to the Earth's location.

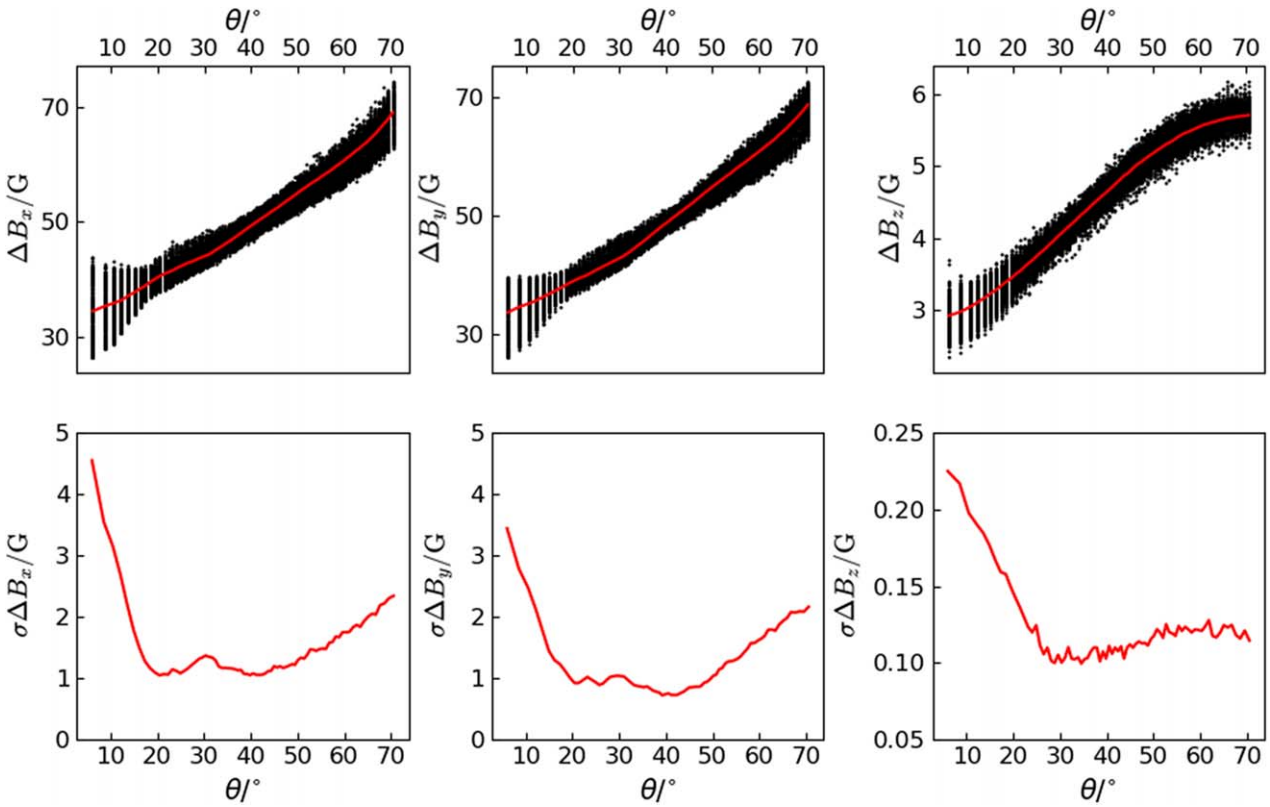

Figure 7. Distribution of magnetic field errors and standard deviations with respect to heliocentric angles is presented. Upper: scatter plot of magnetic field error distribution with heliocentric angles, with the red curve representing the average magnetic field error within 2017. Lower: the standard deviation of magnetic field errors with heliocentric angle distribution curve. The left, center, and right panels respectively display the distribution of ΔB_x, ΔB_y, and ΔB_z. The data are sourced from the HMI website, with one magnetic map collected each day throughout the year 2017.

This allows the corresponding points of magnetic field observations from the three satellites to coincide, achieving a one-to-one correspondence of coordinates for the magnetic field in the common observation area of the three satellites. By substituting the three magnetic maps into Equations (25) and (18), we obtain the values of $\Delta B_{y,\mathrm{new}}$ after precision improvement using the dual-satellite method, the three-satellite method, and the comprehensive method. For the common observation area, the mean values of $\Delta B_{y,\mathrm{new}}$ and the original ΔB_y are computed separately. This yields the distribution of $\mu_y = \frac{\Delta B_{y,\mathrm{new}}}{\Delta B_y}$ with respect to the distribution of the polar orbit satellite on the (φ, θ) plane. Similarly, the distribution of $\mu_x = \frac{\Delta B_{x,\mathrm{new}}}{\Delta B_x}$ can be constructed.

Figure 8 shows that the simulation results, which take into account the distribution of solar magnetic field errors with respect to heliocentric angles, are generally consistent with the results shown in Figure 3, where the error distribution was not considered.

For the polar orbit satellite model represented by the orbital elements, it is challenging to simultaneously display the impact of all parameters on the precision improvement due to the multitude of parameters involved. Figure 9 references the orbital elements of several typical satellites, showcasing the correction effect of the comprehensive method on ΔB_y for different polar orbits. Here, the Earth's initial longitude α_0 is set to $\frac{\pi}{2}$, and the argument of perigee ω is $\frac{\pi}{8}$. The satellite's operation is simulated for a duration of 1200 days, with each simulation step lasting 0.25 days. The parameters for the SO satellite are set as follows: semimajor axis $a = 0.65$ au, eccentricity $e = 0.57$, orbital period 180 days, and orbital inclination $i = 30°$. The parameters for the SPO satellite are set as follows: semimajor axis $a = 1.35$ au, eccentricity $e = 0.26$, orbital period 548 days, and orbital inclination $i = 80°$.

4. Conclusions and Discussions

4.1. Analysis of Simulation Results

Our research indicates that the three-satellite multi-perspective measurement system consisting of Earth, the L5 point, and the polar orbit satellite can enhance the measurement accuracy of each component of the solar transverse magnetic field, effectively resolving the issue of inaccurate transverse field measurements. As shown in Figure 8, both the dual-satellite measurement method and the three-satellite measurement method exhibit similar improvements in the measurement

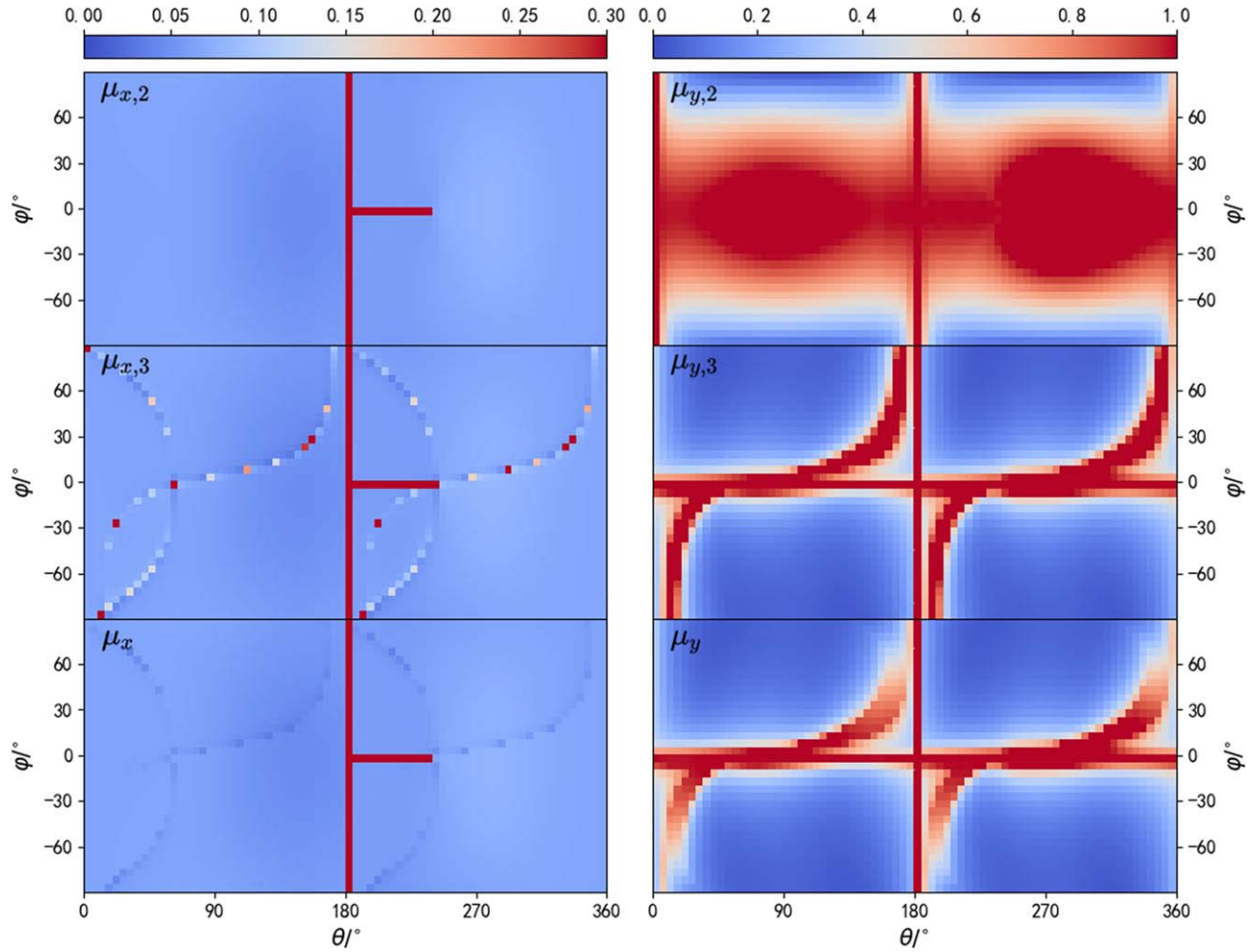

Figure 8. Reduction in magnetic field errors during multi-perspective measurements at different polar orbit satellite positions. φ represents the angle formed by the polar orbit satellite, Earth, and the L5 point; θ denotes the angular distance between Earth and the polar orbit satellite. Left: Improvement in accuracy for B_x, denoted as μ_x. Right: Improvement in accuracy for B_y, denoted as μ_y. Top: μ_2 for the dual-satellite multi-perspective measurement method. Middle: μ_3 for the three-satellite multi-perspective measurement method. Bottom: μ for the comprehensive method, where at each point the method yielding the better result between the dual-satellite and three-satellite methods is chosen.

accuracy of B_x, with the three-satellite method slightly superior. The polar orbit satellite can correct ΔB_x to approximately 10% of its original value across most of the celestial sphere. Regarding the improvement in the measurement accuracy of B_y, the three-satellite method is significantly superior to the dual-satellite method. The polar orbit satellite can correct ΔB_y to around 15% of its original value across most regions of the celestial sphere. However, in some regions, neither the dual-satellite nor the three-satellite method performs well.

From Figure 8, it can be inferred that for higher measurement accuracy of B_y, the polar orbit satellite should be positioned further from the ecliptic plane; otherwise, it cannot provide high-precision observations in the y-direction. Additionally, the angular distance between the polar orbit satellite and Earth should be around 30°–120°. If positioned too close to Earth, the longitudinal component of the polar orbit satellite's magnetic field projected onto the transverse field from the Earth's perspective would be too small, leading to poor multi-perspective measurement effectiveness. Conversely, if positioned too far from Earth, the common observation area would shrink, and due to limb darkening effects, errors within the area would increase. In fact, in the case of an angular distance of 120°, only when the target observation area is exactly in the middle of the two satellites (that is, 60° of the heliocentric angle under the satellite field of view), the limb darkening effects will not significantly affect the measurement accuracy. Under this condition, the available observation area is too narrow. Considering the need to obtain as many observable objects as possible, the angle between satellites should not exceed 90°.

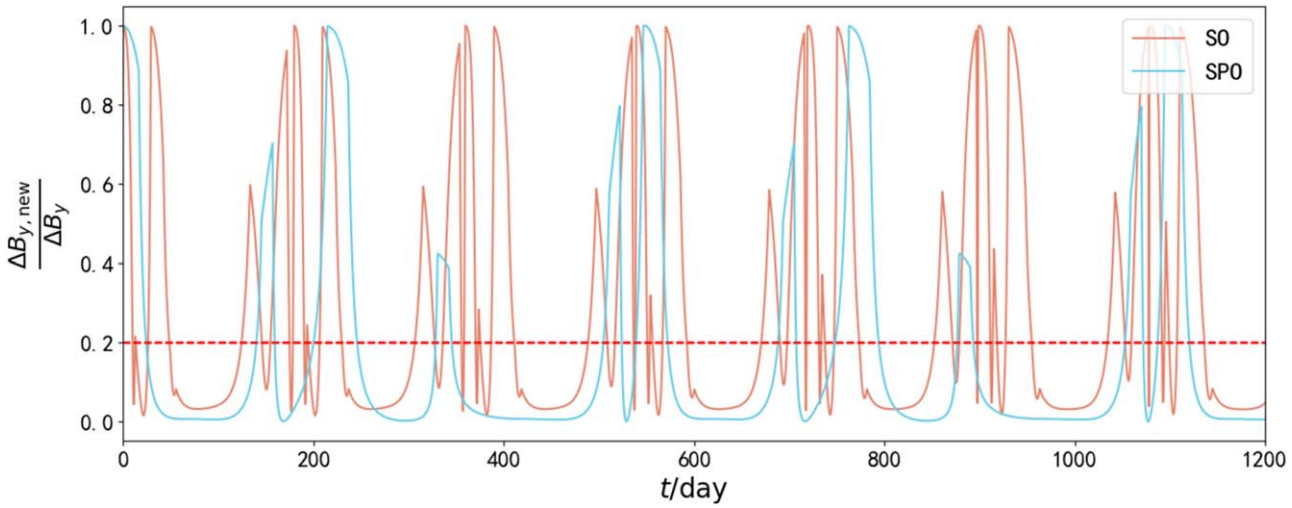

Figure 9. The variation in accuracy improvement effect over time as the polar orbit satellite moves along its orbit.

The orbital simulation results for the polar orbit satellite indicate significant differences in accuracy improvement effects across different orbital configurations. In Figure 9, the SO satellite's average error over the entire simulation period is 30.9% of the original ΔB_y, with 56.7% of the time capable of correcting ΔB_y to 20% of its original value. For the SPO satellite, the average error over the entire simulation period is 17.9% of the original ΔB_y, with 75.5% of the time capable of correcting ΔB_y to 20% of its original value. It should be noted that we only refer to the orbital parameters of SO and SPO, and the error distribution of the magnetic field observations is still provided by the SDO/HMI. The magnetic field error distribution of SO/PHI is different from that of SDO/HMI, and the specific specifications of the magnetic field observation equipment of SPO have not yet been determined.

For a given polar orbit satellite trajectory, the effectiveness of magnetic field error correction exhibits approximately periodic variations over time, alternating between high and low accuracy intervals. This is primarily due to the relative positional relationships of the three satellites repeating certain specific configurations over time. Based on the simulation results, it is reasonable to infer that by appropriately designing the orbital parameters of the polar orbit satellite, the transverse field error can be reduced to approximately one order of magnitude lower than the original, while maintaining high accuracy intervals for more than 80% of the time.

4.2. Errors Caused by the Wilson Effect

Magnetic fields at the same point measured from different perspectives may originate at different atmospheric depths. This is also known as the Wilson effect (Ye 1991). The Wilson effect will introduce new errors in magnetic field measurements. As illustrated in Figure 10, Satellite 1 and Satellite 2 simultaneously observe the magnetic field at point P on the reference plane (height $z = z_0$). Due to the Wilson effect, the magnetic fields they actually observe may be those of points P_1 and P_2 respectively. Then, a new magnetic field error $\Delta B_i = |B(P_i) - B(P)|$, $i = 1, 2$ is introduced. The transverse field error can still be calculated from the longitudinal field errors of multiple satellites by using Equations (16) and (18).

It should be emphasized that, even when using single-perspective measurements, the errors introduced by the Wilson effect still exist. However, in practical applications, this particular error is typically overlooked. Accordingly, in the subsequent steps, we will use the data near the photosphere from a simulation computed by the MURaM code (Chen et al. 2017) to calculate the formation heights of spectral lines under varying viewing angles of different satellites. Additionally, we will estimate the magnitude of the transverse field errors introduced by the Wilson effect in the case of multi-perspective measurements and compare it with the situation of single-perspective measurements.

In this study, we use the RH 1.5D software (Pereira & Uitenbroek 2015) to calculate the formation heights of spectral lines in the photosphere. RH 1.5D is a numerical code for calculating radiative transfer in stellar atmospheres. By solving the radiative transfer equation and the statistical equilibrium equation, it can provide the heights where $\tau_\lambda = 1$ for different spectral lines. We can approximate the height where $\tau_\lambda = 1$ as the formation height of the corresponding spectral line (Qu et al. 1997). The MURaM simulation used in this study, which is the 98x8_hres case in Chen et al. (2017), has a grid of 2048 x 2048 x 512 with a horizontal (vertical) grid spacing of 48 (16) km. We adopt a subdomain of $1024 \times 1024 \times 100$ that covers both sunspots and quiet Sun areas, which is suitable for

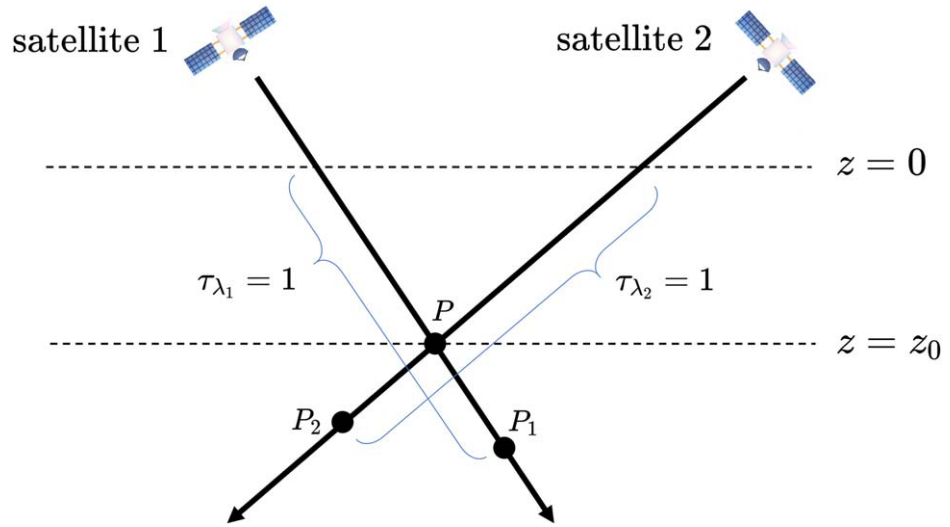

Figure 10. Schematic diagram of the Wilson effect in multi-perspective measurement.

investigating the influence of the Wilson effect in different regions.

RH 1.5D employs a column-by-column calculation method, ignoring the influence of oblique rays. It is suitable for the photospheric layer with a relatively large optical depth. In order to emulate the oblique line-of-sight conditions as observed by satellites, an initial step involves the selection of an observation point P on the reference plane z_0. Subsequently, commencing from point P, the atmospheric model is interpolated into a novel grid along diverse line-of-sight orientations. Through this procedure, the oblique rays detected by satellites can be effectively transformed into vertical rays, thereby rendering them amenable to computation via RH 1.5D. Within the framework of this simulation, eight research domains, each with a dimension of $36 \times 36 \times 100$ (physical scale: 1680 km $\times$ 1680 km $\times$ 1600 km), have been chosen. These encompass four quiet regions and four sunspot areas. For each area, the results at different heliocentric angles (the heliocentric angles of the areas from the perspective of the L1 (or Earth) satellite, ranging from 0° to 60°) are calculated. Considering that the L1 satellite (SDO; Scherrer et al. 2012) and the L5 satellite (LAVSO; Fang et al. 2024) use the 6173 Å spectral line to measure the magnetic field, and SPO (Deng et al. 2023) uses the 5324 Å spectral line to measure the magnetic field, the height of the reference plane z_0 for each area is set as the average formation height of the 6173 Å spectral line within that particular area. Three distinct observation scenarios have been computed individually: single-satellite observation by L1, joint observation by L1 satellite and L5 satellite, and joint observation involving the L1 satellite and the polar-orbiting satellite Sp. With regard to typical cases, the angle of inclusion between the two satellites in the latter two scenarios has been fixed at 60°. The average magnetic field errors associated with different observation points P at varying heliocentric angles have been calculated and are presented in Table 1, where $\Delta B_{\parallel}$ represents the longitudinal field error and $\Delta B_{\perp}$ represents the transverse field error.

It should be highlighted that the magnetic field errors presented in Table 1 merely encompass those induced by the Wilson effect, excluding other measurement errors. As is evident from Table 1, within both the quiet regions and sunspots, the errors attributable to the Wilson effect are of a comparable scale for single-satellite and dual-satellite measurements. By comparing the data in Table 1 with what is displayed in Figure 7, it can be observed that the error values resulting from the Wilson effect are generally inferior to other measurement errors. On the basis of this, it can be reasonably inferred that considering the Wilson effect does not contribute substantially to the enhancement of the accuracy of multi-perspective measurements. In the sunspot region, the degree of variation in the spectral line formation height is more substantial. This leads to relatively larger errors stemming from the Wilson effect within this region. However, given that the magnetic field strength in the sunspot region is also comparatively high, the magnitude of the relative error remains within an acceptable tolerance level. As the measurement region approaches the limb of the solar disk, the line-of-sight becomes increasingly oblique, and the influence of the Wilson effect becomes more pronounced. Consequently, in practical multi-perspective measurement scenarios, the jointly-observed area should be situated as close as feasible to the center of the field-of-view of all satellites. To put it another way, the angular separation between satellites should be maintained at a relatively small value. It should be noted that the absolute magnitude of the error in this simulation is also related to various factors, such as the selection of the reference plane.

Table 1
Magnetic Field Errors Caused by the Wilson Effect

Regions	$\Delta B_{\parallel,L1}$ (Gauss)	$\Delta B_{\perp,L1}$ (Gauss)	$\Delta B_{\perp,L1,L5}$ (Gauss)	$\Delta B_{\perp,L1,\mathrm{SPO}}$ (Gauss)
Quiet Region	0.63	1.00	1.24	2.65
Sunspots	19.66	22.43	21.51	25.41

4.3. Summary and Outlook

Our research provides the general formulas for three-satellite multi-perspective measurements. For other three-satellite systems, one only needs to obtain the rotation matrices between the coordinate systems of the three satellites to use Equations (16) and (18) to determine the transverse field error correction effects. Our study also presents a general method for simulating the transverse field error correction effects of a polar orbit satellite under fixed orbits. For other future polar orbit satellite trajectories, one only needs to input the corresponding orbital parameters to verify the accuracy improvement effects over time.

Compared to the dual-satellite method, the three-satellite measurement method offers superior accuracy improvement effects but also reduces the common observation area and requires more stringent satellite orbital configuration design. Moreover, the three-satellite method only requires each satellite's line-of-sight observation data, eliminating the need for transverse field observation data and thereby reducing instrument costs. In addition, the conclusions presented here do not account for variations in spatial resolution and scale of magnetic field measurement instruments, which may arise due to differences in the satellites' spatial positions. In practical applications, even with identical instruments, the projection effects can alter the spatial scale of pixels, leading to differing measurement effects for the same observation target when using three satellites. Future research can build upon this study, considering factors such as the common observation area size and satellite launch costs, to assess the overall benefits of multi-perspective measurements and further determine the optimal multi-perspective measurement scheme. For future space-based solar observation missions, adopting the multi-perspective measurement method can be considered to enhance the accuracy of magnetic field measurements.

Acknowledgments

The authors thank the NASA/SDO and HMI science teams for providing magnetic field data. Z. M. Z, X. Y. L., Y. G., C. L., and Z. L. are supported by the National Key R&D Program of China (2022YFF0503004, 2020YFC2201200 and 2022YFF0503800) and the National Natural Science Foundation of China (NSFC, grant No. 12333009). Y. G., C. L., Z. L., X. L., F. H., and W. Y. are supported by the National Space Administration of China under the Pre-research Program of Civil Space Technology "Design and Key Technologies of the Solar All-round Stereoscopic Detection System".

References

Borrero, J. M., Tomczyk, S., Kubo, M., et al. 2011, SoPh, 273, 267
Chen, F., Rempel, M., & Fan, Y. 2017, ApJ, 846, 149
Deng, Y. Y., Gan, W. Q., Yan, Y. H., et al. 2020, Infrared Laser Eng., 49 (Tianjin: Tianjin Jinhang Institute of Technical Physics), 230
Deng, Y. Y., Zhang, H. Y., Yang, J. F., et al. 2019, RAA, 19, 157
Deng, Y. Y., Zhou, G. P., Dai, S. W., et al. 2023, ChSBu, 68, 298
Dong, J., & Hu, K. 2019, College Physics, 38, 32
Fang, C., Ding, M. D., Chen, P. F., et al. 2024, AEROSPACE SHANGHAI, 41, 9
Gan, W. Q., Zhu, C., Deng, Y. Y., et al. 2019, RAA, 19, 156
Ji, H. S., Wang, Y. M., & Wang, J. 2019, SCPMA, 49, 44
Karoff, C., Knudsen, M., De Cat, P., et al. 2016, NatCo, 7, 11058
Leka, K. D., Barnes, G., Crouch, A. D., et al. 2009, SoPh, 260, 83
Li, W. X., & Tian, H. 2022, ChJPh, 44, 19
Liu, Y., Hoeksema, J. T., Scherrer, P. H., et al. 2012, SoPh, 279, 295
Metcalf, T. R. 1994, SoPh, 155, 235
Müller, D., Cyr, O. S., Zouganelis, I., et al. 2020, A&A, 642, 642
Pereira, T. M. D., & Uitenbroek, H. 2015, A&A, 574, A3
Qu, Z., Ding, Y., Zhang, X., & Chen, X. 1997, PABei, 98
Scherrer, P., Schou, J., Bush, R., et al. 2012, SoPh, 275, 207
Solanki, S. K., del Toro Iniesta, J. C., Woch, J., et al. 2020, A&A, 642, A11
Solanki, S. K., Inhester, B., & Schüssler, M. 2006, RPPh, 69, 563
Stenflo, J. O. 2017, SSRv, 210, 5
Valori, G., Löschl, P., Stansby, D., et al. 2022, SoPh, 297, 12
Wang, J. J., Liu, S. Q., Ao, X. Z., et al. 2019, ApJ, 884, 175
Wang, J. X. 1994, AcASn, 14, 166
Wang, Y., Bai, X., Chen, C., et al. 2023, AdSpR, 71, 1146
Wiegelmann, T., & Sakurai, T. 2021, LRSP, 18, 1
Yang, M. F., Dai, S. W., Wang, Y., et al. 2022, ChSST, 42, 1
Ye, S. H. 1987, PABei, 5, 3
Ye, S. H. 1991, PPMtO, 10, 92
Zeeman, P. 1897, Natur, 55, 347
Zeng, B. Y., Guo, Y., Li, C., et al. 2024, AcASn, 65, 24
Zhou, R. Y., Ming, W. Y., Na, S. Y., et al. 2021, AcASn, 62, 41
Zhu, X. S., & Wiegelmann, T. 2018, ApJ, 866, 130